Toward quantitative X-ray elastography of coronary arteries using flexural pulse waves

Gregoire, Sibylle; Laloy-Borgna, Gabrielle; Rouviere, Olivier; Giammarinaro, Bruno; Catheline, Stefan

DOI
10.1073/pnas.2419060122

Publication date
2025

Document Version
Final published version

Published in
Proceedings of the National Academy of Sciences of the United States of America

PNAS RESEARCH ARTICLE | APPLIED PHYSICAL SCIENCES

Toward quantitative X-ray elastography of coronary arteries using flexural pulse waves

Sibylle Gregoire[a,1], Gabrielle Laloy-Borgna[b], Olivier Rouviere[c], Bruno Giammarinaro[a], and Stefan Catheline[a]

Edited by David Weitz, Harvard University, Cambridge, MA; received September 20, 2024; accepted March 30, 2025

Dynamic elastography uses an imaging system to visualize the propagation of elastic waves, the speed of which is directly related to the elasticity felt by palpation. Very few studies have focused on X-ray elastography because of the technical challenges it poses: a planar image of an integration volume at a very slow sampling rate. We demonstrate that tracking a slow elastic wave guided along a one-dimensional structure could provide a possible solution. The recently discovered flexural pulse wave, which is naturally generated by heartbeats and propagates along arteries, is the perfect candidate for X-ray elastography. As it reflects the cardiovascular health of patients, arterial elasticity is a biomarker of high clinical interest. We first validate the method by measuring the elasticity in artery phantoms using X-ray. We then move on to data obtained in vivo on coronary arteries during a routine angiography examination. During coronary angiography, a catheter is used to inject an X-ray contrast dye into the patient's aorta. X-rays are then taken as the dye spreads through the coronary arteries. It shows the movement of the coronary arteries for a few seconds and provides an opportunity to follow the natural flexural pulse waves. The obtained Young's moduli for two patients are $E = 38 \pm 30$ kPa and $E = 36 \pm 28$ kPa, respectively. These preliminary results are expected to pave the way for X-ray elastography.

X-ray elastography | arterial elasticity | pulse wave velocity | coronary angiography | quantitative angiography

Significance

The use of palpation is mentioned in the first medical writings dating back 3,500 y. Now known as elastography, this elasticity measurement is used for assessing the stage of liver fibrosis or detecting tumors. Quantitative elastography is based on estimating the velocity of elastic waves that can be detected by medical imaging techniques such as ultrasound, magnetic resonance, or optical imaging. Elastography had never been extended to X-ray imaging, despite being the oldest form of medical imaging. In this paper, we propose a potential solution based on a recently discovered natural elastic wave propagating along arteries: the flexural pulse wave. Applied to X-ray angiography, it may open the way to estimating arterial elasticity, a key parameter of cardiovascular health.

Elastography aims to quantify the mechanical properties of tissues for diagnosis purposes. Dynamic elastography uses an imaging system to visualize the propagation of elastic shear waves, whose speed is directly related to the elasticity of the tissue. Different imaging systems are used depending on the size, the depth, and the resolution required for a specific clinical application. For historical reasons, elastography using ultrasound imaging and MRI have been the main areas of development (1–3). Then, elastography has been developed using optical imaging, thanks in particular to techniques such as optical coherence tomography (4), which provides a high resolution (5). Studies using photoacoustics and microscopes have also been reported (6, 7).

Despite its high spatial resolution and penetration depth, very few studies have focused on X-ray elastography. Indeed, the use of X-ray imaging for elastography presents two major challenges. First, X-ray is a planar imaging technique, the absorption obtained in a scan corresponds to the entire depth traversed by the rays. It is therefore an integrated image where depth has been lost, making it difficult to track longitudinal or shear waves. Second, X-ray is a slow imaging modality, most acquisitions being done between 7 and 15 frames/s (fps) (8). This sampling rate is not adapted to the characteristic times of mechanical waves in biological tissues. However, a few studies have been carried out. Most of them use static constraints to overcome the low sampling rate (9–11). Nevertheless, this static approach does not allow a quantitative estimation of elasticity. More recently, Kamezawa et al made a first attempt into dynamic X-ray elastography (12). As far as the first obstacle is concerned, they used a plane wave in a shallow medium. To overcome the second challenge, they used a stroboscopic approach, with a shear wave source synchronized with the X-ray acquisitions. This approach seems difficult to apply in vivo because of the difficulty of generating plane waves whose propagation axis is contained in the imaging plane.

We propose a quantitative dynamic elastography measurement compatible with the planar aspect of X-ray imaging and its slow imaging rate. To cope with the first difficulty, we choose to study an elastic wave constrained by the geometry of the medium, i.e., a guided wave, which allows propagation to be contained in a plane. X-ray imaging enables deep structures to be seen with good resolution. In particular, it is the gold standard to image deep arteries, where natural guided waves propagate, the so-called pulse waves. Indeed, as a result of the interaction between the heart ejection volume and the arterial

Author affiliations: [a]Laboratory of Therapeutic Applications of Ultrasound, French National Institute of Health and Medical Research, Université Lyon 1, Lyon 69003, France; [b]Department of Imaging Physics, Delft University of Technology, Delft 2628 CJ, The Netherlands; and [c]Department of Radiology, Hôpital Edouard Herriot, Hospices Civils de Lyon, Université Lyon 1, Lyon 69003, France

Author contributions: S.G., O.R., and S.C. designed research; S.G., O.R., and S.C. performed research; S.G., G.L.-B., and B.G. analyzed data; and S.G., G.L.-B., B.G., and S.C. wrote the paper.

The authors declare no competing interest.

This article is a PNAS Direct Submission.

[1]To whom correspondence may be addressed. Email: sibylle.gregoire@inserm.fr.

This article contains supporting information online at https://www.pnas.org/lookup/suppl/doi:10.1073/pnas.2419060122/-/DCSupplemental.

Published April 29, 2025.

tree resistance, a mechanical wave propagates along the arteries, well-known as the pulse wave. In fact, blood ejection during the systolic phase imposes a high pressure at the aorta entry and distends the wall of this artery. This deformation then propagates along the aorta, and being guided by the vessels, will later reach all the arteries of the body. We choose to study these guided pulse waves to estimate arterial elasticity. Estimating arterial elasticity is of great clinical interest. It is a biomarker of atherosclerosis, the phenomenon of hardening of the arteries, which has been shown to be a risk factor for cardiovascular accidents (13, 14).

To tackle the second difficulty, we choose to image a slow elastic wave, slower than both the shear waves and the pulse waves conventionally used. Two types of pulse waves have been observed in the arteries. Indeed, at physiological frequencies (1 to 20 Hz)(15), only a few modes of propagation can exist. The axisymmetric mode, that has been extensively studied (16–18), has a speed which depends on the elasticity according to Moens–Korteweg's formula (19, 20). It is too fast to be followed with X-ray. The flexural mode has been recently observed in the carotid and in the retinal arteries (15). The source of this flexural mode is the heartbeat. It can come both from the heart itself, which is a nonperfectly symmetrical source, and also from the mode conversion of the axisymmetric pulse wave due to symmetry breaking along the wave path. In addition, vibrations due to heartbeat occurring in the surrounding soft tissues can be guided along the blood vessels in the form of flexural waves. It has a speed which depends on the elasticity according to a dispersive law (21) and is around ten times slower than the axisymmetric mode at physiological frequency. Because of its guided nature and slow speed, it is the perfect candidate for dynamic X-ray elastography.

A controlled set-up is first used to follow flexural waves with an X-ray imaging system in artery phantoms of known elasticity. The results obtained are compared with a similar optical set-up used at a higher sampling rate. Then, in order to observe the propagation of flexural pulse waves in vivo, we used data from a routine clinical examination: coronary angiography. During coronary angiography, an X-ray contrast dye is injected in the patient's aorta using a catheter. X-ray images are recorded as the contrast dye flows into the coronary arteries. Contrast dye highlights potential luminal narrowing indicating stenosis. If necessary, stenting is performed using X-ray guidance (22). We propose to provide a costless additional measurement: the average elasticity of the patient's coronary arteries. In other words, flexural pulse waves imaging allows us to perform in vivo quantitative X-ray elastography, on deep internal structures: the coronary arteries. Coronary angiographies from two patients are studied and quantitative global measurement of coronary arteries elasticity is performed.

Results

Phantoms Experiments. First of all, we want to ensure in a controlled set-up that by imaging flexural waves using X-rays, we are able to determine elasticity. The experimental set-up is displayed in Fig. 1*A*. A polyvinyl alcohol (PVA) artery phantom is immersed in water and filled with X-ray contrast dye. A shaker is placed in contact with the phantom edge. A radiography dynamic system is used. A water tank containing the filled tube is placed on a flat panel detector below an X-ray source. X-ray images are acquired at 15 fps. Fig. 1*D* is an example of a frame, the contrast dye inside the tube is revealed in white. To have a comparison, a similar optical set-up previously used to study flexural wave (21) is used at higher frame rate to assess ground truth. This twin set-up as shown in Fig. 1*A*, uses a CMOS camera at 45 fps to register the same artery phantom placed in a water tank upon a lighting table. Fig. 1*B* is an example of a frame, the external edges of

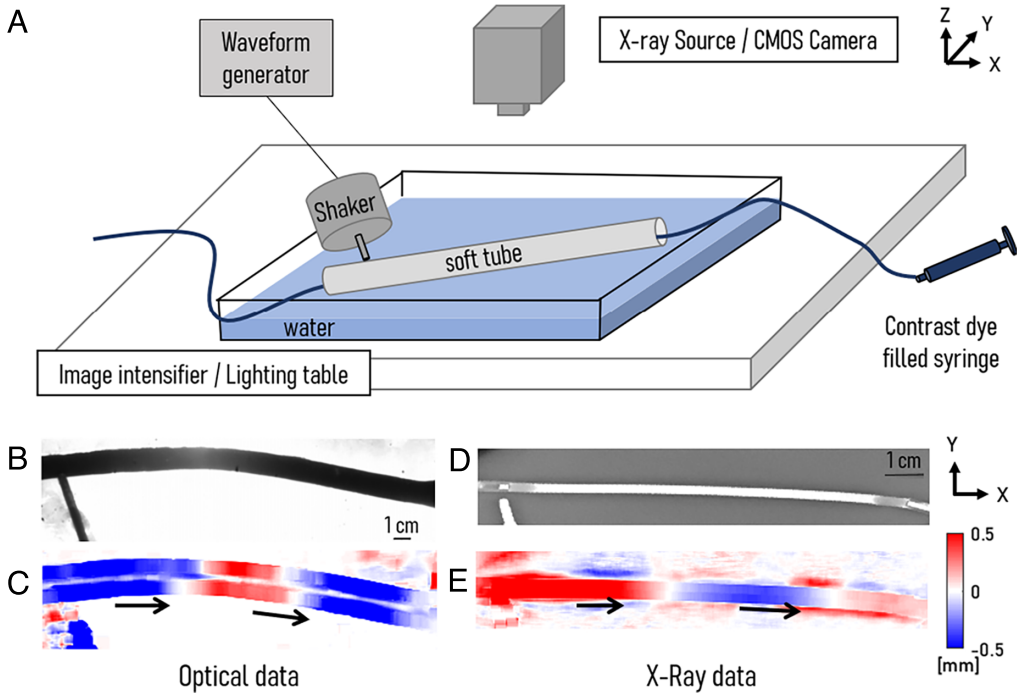

Fig. 1. (*A*) Schematic diagram of experimental set ups. An artery phantom is immersed in water and filled with X-ray contrast dye. A shaker, driven by a waveform generator, is placed in contact with the artery phantom. Depending on the set-up considered, an X-ray source and its image intensifier are used at 15 fps, or a CMOS camera at 45 fps and a lighting table. (*B*) Raw optical image and (*C*) the corresponding field of displacements. (*D*) Raw X-ray image and (*E*) the corresponding field of displacements. Black arrows indicate the direction of the wavefronts.

the artery phantom in black contrast with the background light. Details can be found in *Materials and Methods*.

To compute the displacement field from the raw image stack, we use the Lukas and Kanade differential approach (23) to estimate the optical flow. It allows us to retrieve the displacement field in X and Y direction for each time step, as displayed for the Y direction at an exemplary time in Fig. 1*C* for optical data and Fig. 1*E* for X-ray data. Black arrows indicate the displacement direction; several wave fronts can be distinguished. X-ray and optical raw data movies and their corresponding displacement videos are given in *SI Appendix*. In both cases, the guided flexural wave can be seen meandering along the tube. Only displacements in the Y direction are considered and displacements along the tube are averaged over the normal to the tube axis. We obtain a displacement field dependent on a single spatial coordinate, X.

To compute the phase velocity of the flexural waves in the artery phantom, we use an approach derived from seismology and passive elastography (24–27). For each frequency, the cross-correlation of the Fourier transform of the field is computed. It can be interpreted as the point spread function of the medium. Correlation measurement enables to measure the wave velocity using the complex wave field composed of the incident wave and its potential reflections (28). Details can be found in *Materials and Methods*. The cross-correlations $C(f,x)$ map, where each line corresponds to averaged spatial cross-correlation at one frequency, is displayed in Fig. 2*A* for optical data and Fig. 2*B* for X-ray data. We expect the wavelength to diminish as the frequency increases. This trend can be clearly seen in the X-ray and optical data. To obtain a dispersion curve, we calculate the cross-correlations over all the frequencies generated by the shaker.

The wavelength (λ) at each frequency (f) is estimated by taking the maximum of the spatial Fourier transform of each cross-correlation $C(f)$. The product gives the phase velocity $V_\phi = \lambda f$. The obtained dispersion curves for X-ray data and optical data are plotted Fig. 2*C*. Red and black crosses are experimental values. There is a rather good agreement between the velocities derived from the X-ray data and those derived from the optical data. X-ray imaging at 15 fps seems to be able to measure the velocity of flexural waves, in the same way as a camera.

To link the propagation of guided flexural waves to the elasticity of the phantom, one needs a propagation model linking the velocity of the waves to the Young modulus of the phantom. At the physiological frequencies naturally present in arteries (1 to 20 Hz) (15), it has been shown that the propagation of flexural waves in arteries can be approached by a new model derived from the Euler Bernoulli beam theory (21). This model is only valid if the propagation frequency is below the ring frequency of the phantom, 15 Hz, which is our case. According to this model, the phase velocity of the flexural pulse wave, v_F, states as Eq. **1** where f is the frequency, h the thickness of the arterial walls, r its radius, E its Young modulus and ρ its volumetric mass. The dependence of speed on the square root of frequency explains why speed tends toward zero at low frequencies. Thanks to this model, measurements of the phase velocity of the flexural pulse wave allow the elasticity to be estimated if the geometrical parameters are known.

$$v_F \approx \sqrt{2\pi f \sqrt{hr}\sqrt{\frac{E}{\rho}}}. \qquad [1]$$

In order to estimate the elasticity of the tube with both datasets, we fit this model to the dispersion curves acquired experimentally. The plain red and black curves in Fig. 2*C* are the fits to optical and X-ray data of the new model derived from Euler–Bernoulli beam theory. Experimental velocities and the theoretical propagation model seem to follow a similar trend. For X-ray data, the Young modulus obtained by the fit is $E_X = 58 \pm 8$ kPa. For optical data, the Young modulus obtained by the fit is $E_{optic} = 50 \pm 7$ kPa.

In vivo, arteries are curved and pulse wave propagation takes place along this curved axis. To check that our measurement was robust to curvature, a second, longer, and softer tube was studied in a similar way. The results can be found in *SI Appendix*, Figs. S1 and S2. The propagation axis of this phantom is curved,

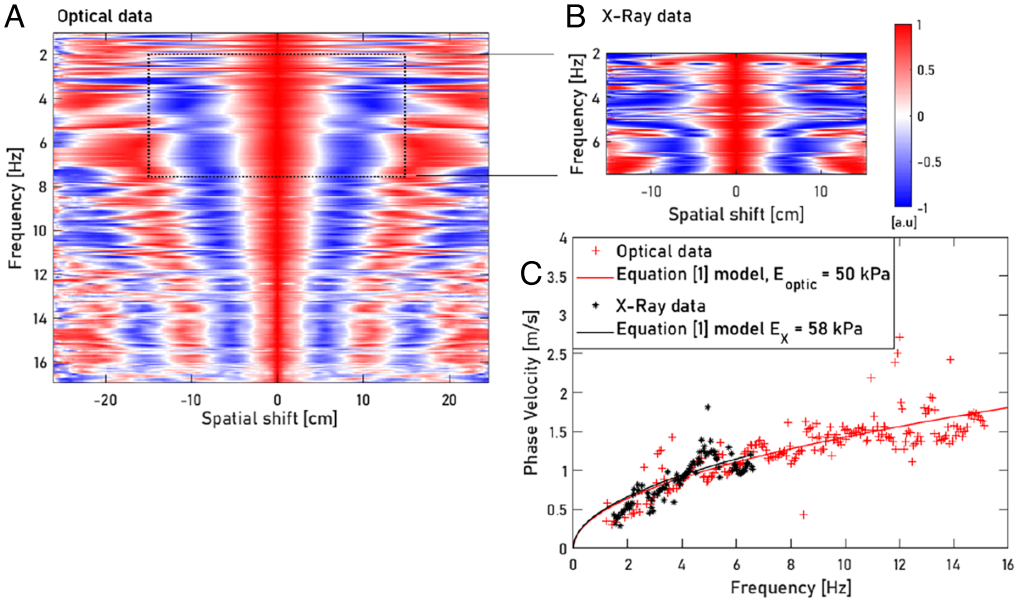

Fig. 2. Cross-correlation of the displacement field in the artery phantom , $C(f)$, for all frequencies for (*A*) optical imaging, (*B*) X-ray imaging. (*C*) Dispersion curves derived from the cross-correlations with optical imaging (red crosses) and X-ray imaging (black crosses). Solid lines represent the fit of the data with Eq. **1**, the flexural wave propagation model developed in article (21). $E_{optic} = 50 \pm 7$ kPa is obtained via data acquired in optical imaging and $E_X = 58 \pm 8$ kPa in X-ray imaging.

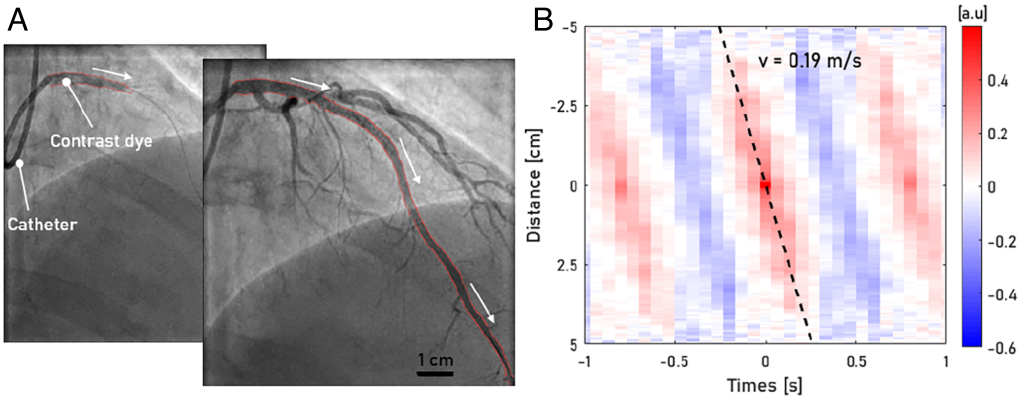

Fig. 3. (*A*) Frame acquired after 0.27 s (*Left*) and 1.33 s (*Right*) of the postoperation angiogram of case study (29). White arrows indicate the propagation direction of the dye. (*B*) Spatiotemporal representation of the experimental displacements using normalized correlation. Black line corresponds to the wave velocity measurement using the time-of-flight technique.

so propagation does not take place along X or Y. At each point on the propagation axis, the normal to this axis is found. Then the X and Y displacements are projected onto this normal. Finally, the normal displacements obtained in the tube section are averaged. The dispersion curves are calculated using the same correlation method described above. $E_{optic} = 21 \pm 5$ kPa is obtained via data acquired in optical imaging and $E_X = 16 \pm 5$ kPa in X-ray imaging. By comparing the moduli obtained by X-ray on the 2 phantoms studied with the optical reference data, we obtain an average error of 20%.

This experiment demonstrates on a controlled set-up the possibility of quantitative X-ray elastography. Due to their guided nature and low-frequency dispersion, flexural waves can be used for X-ray elastography. With a view to applying this method in vivo, it should be remembered that flexural waves have been observed in the carotid artery and even in the microcirculation of the retinal arteries (15). They are thus also present in the coronary arteries. Therefore, at this stage, we are seeking to apply the same method in vivo, to quantify the elasticity of the coronary arteries, using X-ray imaging at 15 fps. To do so, we use data acquired during a routine examination, coronary angiography.

X-Ray Elastography of Coronary Arteries. During coronary angiography, an X-ray contrast dye is injected into the patient's aorta using a catheter. Scans are acquired as the fluid spreads through the coronary arteries. It allows the artery to be visualized and the displacement on its surface to be estimated for a few seconds. Our aim is to extract from these displacements the propagation velocity of flexural pulse waves.

Two case studies are considered (29, 30). They were selected because coronary angiographies are acquired at high frame rates, 15 fps. In case study (29) two coronary angiograms were performed, before and after angioplasty. Specifications can be found in *Materials and Methods*. The three coronary angiograms studied are available as *SI Appendix* of articles (29, 30). Fig. 3*A* displays two frames acquired on the angiograms of patient (29) after his operation.* Many objects can be seen in the frames. The vertebral column can be seen on the left, as well as two ribs. The thoracic diaphragm can be seen on the right. It illustrates the difficulty of working with an imaging device that provides an integrated quantity on a volume. The contrast dye filled catheter appears on the upper left part of the frame. The contrast dye makes the artery stand out from other structures. The white arrows indicate the direction of its spreading. An artery of interest is selected and highlighted in red. Breathing and heart muscle movements cause the artery to move within the X-ray field of view. These overall movements need to be filtered out from the artery displacements. To do so, the artery of interest is isolated in each frame using a semiautomatic detection algorithm previously used in other work (15). A curvilinear abscissa is defined along the artery of interest, originating at the junction with the catheter. Thus, each point is identified by its distance from the catheter. This allows us to locate a point along the artery even if it moves in the field of view from frame to frame. For each frame, the normal to the curvilinear abscissa is calculated for each point of the curvilinear axis. Then, the displacements of the arteries are calculated using the same optical flow method used for the phantom experiment. For each point of the curvilinear axis, the displacements are projected onto the normal to the axis at that point. Finally, normal displacements are averaged along the cross-section of the artery. This procedure is repeated for each frame. The result is a displacement signal with a single spatial dependency. Fig. 3*B* is a spatiotemporal representation of the displacements using normalized correlation shifted in time. A slope, indicating propagation, is clearly visible, allowing us to make an initial estimate of the wave's speed using the time-of-flight method. Using a linear fit, the group velocity of this wave is estimated at $v = 0.19$ m/s. This is a first approximation of a group velocity, which gives us an order of magnitude of the observed speeds. However, because of the dispersion of the guided flexural wave, we prefer to use a spectro-correlation approach rather than time-of-flight measurements. Indeed, the issue is similar to the phantom experiment presented above: we want to characterize waves with a 1D in space signal and a frame rate of 15 fps.

The spectrum of the temporal correlation of the displacement field of the postoperation angiogram of the case study (29) is shown in Fig. 4*A*. As the heart emits a temporal signal that is periodic at the heart rate, this has a sampling effect on its spectrum. A dirac comb at the heart rate is applied to the spectrum, which explains the peaks observed in Fig. 4*A*. The patient had therefore a heart rate of 1.3 Hz (78 bpm). To ensure a good signal-to-noise ratio, as well as to avoid potential spectrum aliasing effects, only the four dominant peaks are considered. The cross correlation $C(f)$ is only computed at the four frequencies circled in Fig. 4*A*; results are displayed in Fig. 4*B*. Once again, the cross-correlation can be interpreted as the point spread function

* To make it easier for the reader to find these data, possible links to these resources are given here. For ref. 29, https://www.icrjournal.com/video-index/coronary-angiography-left-coronary-artery, https://www.icrjournal.com/video-index/post-procedural-angiography. For ref. 30, https://www.youtube.com/watch?v=HKXTZUYTxkA.

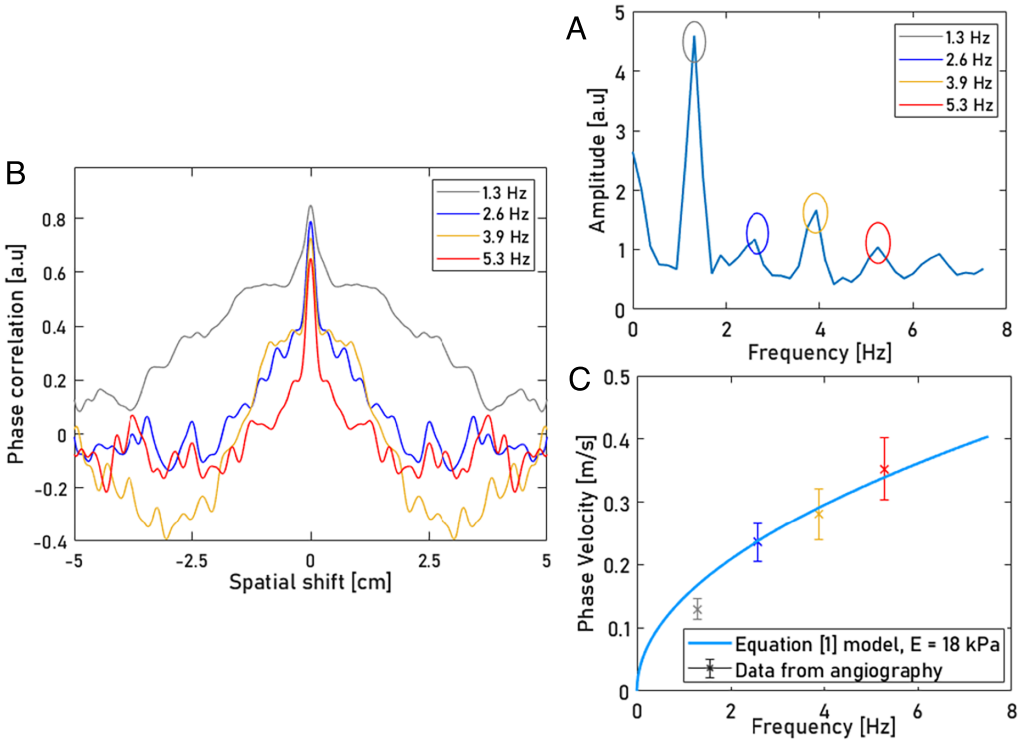

Fig. 4. (*A*) Spectrum of the temporal correlation of the displacement field obtained from the post operation coronary angiogram of case study (29). The four circled peaks correspond to the first heart rate multiples. (*B*) Cross-correlation $C(f)$ of the displacement field, only heart rate multiples are studied. (*C*) Crosses are experimental phase velocities derived from the cross-correlations. The plain blue curve is the corresponding fit of the new model of flexural wave propagation derived from the Euler–Bernoulli beam theory (Eq. **1**).

of the medium. For a 1D signal, it is a sinusoid whose wavelength is that of the wave in the medium. We observe that the cross-correlation becomes narrower as the frequency increases. The wavelength decreases with increasing frequency, as expected. For the four cross-correlation profiles $C(f)$, a sinusoidal fit is performed to obtain the wavelengths at each frequency. The phase velocities $V_\phi(f)$ are then computed. Results are displayed as crosses in Fig. 4*C*. More details about the error bars can be found in *Materials and Methods*.

The magnitude of the velocity observed in Fig. 4*C* is too small to correspond to longitudinal or shear waves as well as axisymmetric pulse waves. Indeed, longitudinal or shear waves are traveling above 1 m/s in soft tissue. In particular, shear waves in the myocardium travel at speeds greater than 1 m/s (31, 32). It cannot be an axisymmetric pulse wave either. To our knowledge, it has never been measured in the coronary arteries, but in the carotid artery, it travels at a speed largely above 1 m/s (33). What's more, if these were axisymmetric waves, the order of magnitude of the elasticity found would be far too low. At last, a dispersive behavior is clearly observed in Fig. 3*C*. This dispersive behavior on a narrow frequency band excludes both longitudinal and shear waves as well as axisymmetric pulse waves (15). All these elements suggest that we are indeed detecting a flexural wave.

As in the phantom approach, we seek to derive a Young's modulus using a propagation model for flexural pulse waves. We are in the frequency domain of validity of the new model of flexural pulse wave propagation derived from the Euler–Bernoulli beam theory (Eq. **1**). We approximate the geometric parameters of the artery of interest by calculating the mean radius r_m and by approximating the mean arterial thickness h as 0.8 mm, the mean in the population (34). By fitting the propagation model (Eq. **1**) to the data, we give an approximation of the Young modulus. The result is displayed in Fig. 4*C*, the plain blue curve is the prediction of the model for an artery of $r_m = 1$ mm, $h = 0.8$ mm and $E = 18$ kPa.

The same method is applied to the other coronary angiographies. Results are displayed in *SI Appendix*, Figs. S3–S5. For patient 1, the two estimations on pre/post operation angiograms are performed on the same artery (the left anterior descending artery). For patient 2, two arteries are processed on the same angiography. We consider only three dominant peaks in the spectrum, the first being at the heart rate (f_{heart}). For each frequency peak, the corresponding phase velocity, $V_\phi(f)$, is calculated. The results are displayed in Table 1. For sake of

Table 1. Results of elasticity estimations on patients of case study (29, 30)

	Ref.	f_{heart} (Hz)	$V_\phi[f_{heart}]$ (m/s)	r_m (mm)	E (kPa)
Patient 1 preoperation	(29)	1.6	0.48 ± 0.06	1.0 ± 0.2	58 ± 46
Patient 1 postoperation	(29)	1.3	0.13 ± 0.02	0.8 ± 0.2	18 ± 14
Patient 2 artery 1	(30)	0.8	0.15 ± 0.02	0.9 ± 0.2	15 ± 12
Patient 2 artery 2	(30)	0.8	0.10 ± 0.01	1.1 ± 0.2	56 ± 45

f_{heart} is the heart rate of the patient during examination, it corresponds to the first frequency selected to compute the phase velocity V_ϕ. r_m is the mean artery radius. Young modulus is retrieved by fitting on the data the new model of propagation derived from Euler–Bernoulli beam theory (Eq. **1**) describing the propagation of flexural pulse waves in arteries.

clarity, only the phase velocity values computed at the heart rate are shown but complete results are available in *SI Appendix*, Table S1. It can be seen that in all the angiograms processed, the order of magnitude of the phase velocity found is the same. In the case of patient 1, the measurement was taken before and just after a stenting operation on the artery. Our results seem to suggest that the artery softened slightly after the operation, but our error bars do not rule out constant elasticity. In view of the short timescales involved, we do not expect any immediate effects on the elasticity of the artery, and the overall elasticity should not, in principle, be affected. This highlights that this study gives an idea of the expected elasticity but does not allow us to conclude on a possible change in elasticity due to high error bars. Overall, the estimated Young's modulus of the coronary arteries of patient 1 is $E = 38 \pm 30$ kPa that of patient 2 is $E = 36 \pm 28$ kPa.

Discussion

The experiment on arterial phantoms shows rather good agreement between X-ray imaging elasticity measurements and those obtained with an optical setup used as control for both phantoms studied. We obtain a 20% error per X-ray by taking the optics as the reference value. Flexural wave imaging overcomes the difficulties associated with X-ray elastography, the slow sampling rate and the integration of a volume on an imaging plane. It demonstrates in phantoms the possibility of quantitative X-ray elastography.

In vivo, using data not designed for our application, a wave propagating along the coronary artery is detected. This wave is too slow to be a longitudinal or shear wave or an axisymmetric pulse wave but is consistent with that of a flexural wave. Furthermore, we show a frequency dependence of the phase velocity relevant for a flexural wave. Thanks to a propagation model developed for flexural waves in arteries, a quantitative estimate of the elasticity of coronary arteries is now possible, although the precision still needs to be improved. This approach to quantitative X-ray elastography is based on a noninvasive method already used in clinical practice.

The obtained Young's moduli for the two patients are $E = 38 \pm 30$ kPa and $E = 36 \pm 28$ kPa, respectively. In diseased and ex vivo coronary arteries, the order of magnitude obtained varies: in biaxial mechanical testing, Kural et al. (35) obtained between 50 and 210 kPa; in uniaxial testing, Karimi et al. (36) obtained 1 MPa. In biaxial testing, Guo et al. (37) obtained 1 MPa, a value they compared with 200 kPa an intravascular ultrasound-based modeling estimation from a healthy volunteer. It seems difficult to compare our values with the literature, as we are not aware of any dynamic in vivo estimates. This is why we prefer to compare our values with dynamic measurements taken on the carotid artery, bearing in mind that it is at least twice as wide. As the carotid artery is easy to image using ultrasound, its elasticity has been extensively studied. Using shear wave elastography, Wang et al. (38) found an average elasticity of 45 kPa in 169 healthy patients. Using the symmetrical pulse wave, Lou et al. (18) found 50 kPa, and using the flexion pulse wave our team (15, 21) found 40 kPa. The order of magnitude of our measurements is consistent with in vivo measurements taken on a larger artery, the carotid artery. To our knowledge, no dynamic in vivo elasticity measurements are available on the coronary arteries. Our estimate leads the way.

The main improvement to be made to the measurement is to move from a 2D projection of the artery to a 3D visualization. Indeed, X-ray imaging only provides a planar image of a 3D structure. Coronary arteries are not contained within the imaging plane. It induces an error in the distance measurement along the curvilinear abscissa. The measurement error on the elasticity is estimated at 50% based on the angle between the actual plane of the artery and the imaging plane. Main sources of error in the measurement are the estimation of the thickness of the artery, the radius of the artery and, above all, the estimation of the distance traveled by the wave. Taking all the sources of error together, we estimate the error on the Young's modulus to be 80%. The full uncertainty calculation can be found in *Materials and Methods*. To know the true length of the coronary, we need a 3D reconstruction. This is not a major constraint because angiography is usually repeated in clinic with different views by rotating the imaging plane (39). Improvements in the estimation of the geometric parameters of the artery are also being considered, such as the use of complementary intravascular ultrasound echography examination to estimate the average thickness of the artery walls (40).

Other improvements could be envisaged. The number of frames on which the entire artery is visible could be increased. This could be achieved by slightly modifying the way radiologists work. During our phantom experiments, because of a contrast agent leak in the water tank in which the phantom was immersed, we observed that we were able to follow waves even with a very diluted contrast agent. By injecting the same quantity of contrast agent two or three times more slowly, this could double or triple the number of frames over which the entire artery is visible. Increasing the recording length offers many possibilities:

- Longer acquisitions would improve the signal-to-noise ratio. It would allow phase velocity measurements to be made at more multiples of heart rate than three. It would thereby increase the number of points on which the fit of the flexural wave propagation model is based.
- Longer visualization of the entire artery could allow us to work with angiograms acquired at lower sampling rates than 15 fps to better match clinical practice of recording between 7 and 15 fps (8). In fact, with a longer signal at a lower sampling rate, we may be able to obtain a measurement point at the heart rate with a sufficient signal-to-noise ratio.
- The flexural wave propagation model (Eq. **1**) assumes linearity between stresses and strains. However, as the flexural wave passes through the arteries, the heart contracts, stretching and relaxing the artery. Furthermore, when the symmetrical pulse wave passes through the artery, the strain imposed onto the vessels' walls modulates their elasticity (through the nonlinear acoustoelastic effect). Longer acquisitions could enable us to eliminate frames corresponding to nonlinearities to perform the measurement of flexural wave velocity.

By enabling elasticity to be measured using X-ray imaging, flexural waves open the door to advances in the field of coronary angiography. Quantitative coronary angiography (QCA) is a major research branch in the field of coronary angiography. It aims to produce quantified indices from the angiographic examination. QCA was developed because visual estimation of stenosis severity is unreliable (41, 42). QCA also plays a major role in the evaluation of interventional techniques (balloon angioplasty, stenting) and in the development of new devices such as drug eluting stents. The main parameters studied are lumen loss and stenosis diameter (22). To assess these parameters, image processing algorithms have been developed to segment the artery and reconstruct its shape (43–45). These algorithms could be

applied in our case to better segment the artery and improve the signal-to-noise ratio. Another relevant indicator studied in QCA is the pressure drop before and after stenosis, which is called angiography derived fractional flow reserve (angio-FFR) (46). Computational fluid dynamics is used to simulate pressure profiles associated with angiograms and derive the pressure drop. These algorithms have the same specifications as those required for flexural wave elastography. They rely on 3D reconstruction of the arterial tree geometry based on different angle angiographies, as well as on a high frame rate of 10 to 15 fps (47). Combined with 3D QCA, or dataset used in angio-FFR, flexural pulse waves could provide a costless local elasticity measurement, which has been proven to be a biomarker of cardiovascular accidents (13, 14).

To summarize, this work provides a proof of concept for quantitative elastography using X-ray imaging. The goal is to assess a biomarker of cardiovascular accidents, the elasticity of arteries, using a wave naturally present in blood vessels, the flexural pulse wave. This wave is both guided, which is compatible with the property of absorption over a volume of X-rays, and slow, which is compatible with the slow frame rate of X-ray imaging. We show that it is possible to recover the elasticity of an artery phantom using X-ray imaging. A rather good agreement is obtained with an optical reference set-up. We then apply the same method in vivo to data from a routine examination, coronary angiography, carried out during two different clinical case studies. This allows us to make a quantitative in vivo measurement of X-ray elasticity, despite a nonnegligible margin of error. We propose a potential dynamic elastography measurement of the coronary arteries, which has no equivalent in the literature. This work opens up many new perspectives. In the field of coronary imaging research, the prerequisites for X-ray elastography are the same as those for techniques currently in research (3D QCA, angio-FFR). There are no limitations to the use of arterial elasticity as a biomarker of coronary disease. X-ray elastography using flexural waves also has potential applications outside the scope of coronary arteries. Slower, guided waves can be followed in other structures than arteries. Other blood vessels could also be investigated. For instance, pulmonary angiograms or cerebral angiograms could be considered. To sum up, the use of flexural pulse waves opens up great possibilities for the field of coronary angiography as well as for elastography in general.

Materials and Methods

PVA Phantom. 10% PVA, (Sigma Aldrich, 363146-500G) is heated until dissolution and mixed with 1 % of graphite powder (Fisher Chemical) under constant stirring. The mixture is then degassed under a vacuum chamber. It is poured into a home-designed mold in polyvinyl chloride. The filled mold is then submitted to two freezing cycles (12 h at room temperature, 12 h in freezer). Phantoms are removed from the mold and stored into water at room temperature. The artery phantom of Figs. 1 and 2 is 25 cm long, has an outer radius of 7 mm and a wall thickness of 3 mm. The second artery phantom presented in *SI Appendix* has the same outer radius and wall thickness but is 35 cm long.

X-Ray and Optical Set-Up. In the case of the X-ray set-up, a radiography dynamic remote-controlled system (Stephanix, D^2RS) is used. A water tank containing a polyvinylalcohol phantom is put on the image intensifier under the X-ray source. The optical set-up is composed of a camera (Chronos 1.4), equipped with a zoom lens (Computar M6Z1212-3S), which focuses on the polyvinylalcohol phantom inside the water tank put on a lighting table (Intimus 2008). The tube is filled with X-ray contrast dye (Visipaque 320 mg I/mL). For data of Figs. 1 and 2, the shaker (The Modal Shop K2004E01), is controlled by a waveform generator (RS Pro RSDG805) to send vibrations between 3 to 7.5 Hz. For the first phantom, the X-ray pixel size is 0.285 mm, the optic pixel size is 0.280 mm. For the second phantom presented in *SI Appendix*, the shaker sends vibrations between 3 and 7.5 Hz for X-ray data and between 3 and 20 Hz for optical data. The optic pixel size is modified due to magnification to 0.260 mm, the X-ray pixel size remains 0.285 mm.

Displacement Field Estimation. To calculate the displacement field at each point in space, we use the differential optical flow estimation approach proposed by Lukas and Kanade (23). The raw data are spatially smoothed by means of an average filter of 30-pixel for phantom optical data, 20 pixels for phantom X-ray data and 15 pixels for angiography data. By comparing successive images in pairs, we obtain the 2D displacement field over time. To estimate the displacements normal to the propagation of the flexural wave, for each point on the curvilinear axis, we project the components onto a unit vector normal to that axis. We start by finding the two contours of the studied artery or phantom and defining the curvilinear abscissa along these contours. Then, the vector normal to the contours is calculated at each point and the displacement field is projected onto this vector. Finally, the average of the projected displacement on the two contours is calculated for each value of the curvilinear coordinate.

Phase Velocity Estimation. To compute the velocity of the flexural waves, one first needs to filter out the axisymmetric wave contribution from the displacement signal. For this purpose, an approach similar to the one used in ref. 15 is used, consisting in summing the displacement signals of the two vessel walls. Indeed, the displacement signals of the two vessel walls associated to an axisymmetric deformation are opposite numbers, whereas they have the same sign in the case of a flexural deformation. Hence, by summing the displacements over the vessel cross-section, only the flexural contributions to the displacement signal are selected. Once the flexural mode selected, we use an approach derived from seismology and passive elastography to measure the phase velocity. The displacement field's cross-correlation is interpreted as the field's point spread function (48, 49). The aim is to calculate the dispersion of a guided wave from its displacements, i.e its phase velocity as a function of frequency. To obtain frequency-by-frequency information, we use the Fourier transform of the displacements, $\phi(f,x)$. The cross-correlation of the Fourier transform of the field, $C(f,x)$ is calculated using Eq. **2**, with x being the curvilinear axis, f the frequency, and δ a space shift sweeping along this axis. To whiten the data, only the phase of cross-correlation is taken into account.

The cross-correlation $C(f,x)$ is computed for each point x and a spatial mean $C(f)$ is computed for each frequency. Calculations are therefore performed using

$$Re(C(f,\delta)) = Re\left[\langle \frac{\phi(f,x+\delta)^*\phi(f,x)}{|\phi(f,x)||\phi(f,x+\delta)|}\rangle_x\right], \quad [2]$$

which yield for one-dimensional propagation with a wave vector k, to

$$Re(C(f,x)) \approx \cos[k\delta]. \quad [3]$$

This spatial mean of cross-correlations can be interpreted as the point spread function of the medium. For a wave guided in a 1D structure, such as a pulse wave in an artery, the point spread function is a sinusoid whose wavelength is that of the wave in the medium (28).

For phantom experiments, the wave vector is estimated for each frequency as the maximum of the spatial Fourier transform of the correlation. A zero padding of 1,000 points is used. To avoid potential spectrum aliasing in X-ray data, a low-pass filter is applied in the k-space to filter out the folded high spatial frequency by removing high wave number. We use the well-sampled optical data to determine the cut-off frequency.

For in vivo data, the spatial Fourier transform method is not feasible due to the low number of frames per acquisition. A nonlinear least square regression using a cosine function is performed on the correlation at each frequency to obtain the wavelength at each frequency. Before the fit, we apply a low-pass filter with a normalized cut-off frequency of 0.01 πrad/sample to smooth out spatial correlations.

The Young's modulus is obtained by a nonlinear fit of Eq. **1** to the dispersion curves. For the experimental data, the error bar is approximated as the 95% CI of this fit.

Time-of-Flight Velocity Measurement. The usual time-of-flight method uses a spatiotemporal representation of the experimental displacements and computes the slope to retrieve the wave velocity (50). In this work, the spatiotemporal representation is based on the temporal correlation of each space line with increasing time delay; a full description can be found in ref. 15. Then, each temporal signal is upsampled up to 100 times using "spline cubic" interpolation. The maxima of each time-series are then determined and then processed using a linear regression. The slope yields the group velocity as shown with a black-dashed line in Fig. 3*B*.

Estimation of the Mean Radius of the Arteries. In all the angiographies considered, the 2 mm wide catheter is used as a spatial scale. To estimate the mean radius (r_m) of the artery, the first part of the artery is considered significant, as it is always illuminated by the contrast agent. The radius is calculated in each point of the artery using the cross-sections of the arteries. The values obtained are then averaged over the part of the artery illuminated by the contrast agent throughout the angiography, in a window of comparable size to the wavelengths of the flexural wave. The SD of this value is around 20% in all the angiographies studied.

Clinical Case Study Specifications. In case study (29) the patient is a 47-y-old woman with recurrent chest pain. Two coronary angiograms were performed, the first revealing a stenosis, the second acquired after placement of a stent on this stenosis. In case study (30) the patient is a 32-y-old man experiencing acute chest pain. The coronary angiography was made during the diagnosis process of a chronic inflammation of the gallbladder.

Uncertainty on In Vivo Estimation. The main error in measuring the wavelength at one frequency comes from the error on the distance. X-rays produce an image of a volume, so the artery may not be contained within the plane. An error is therefore made on the curvilinear abscissa measured. During an angiography, the radiologist chooses an imaging plane in order to have a good view of a specific artery. Given the different views possible (51), we estimate that there is a maximum angle of $\pi/6$ between the plane of the artery and the imaging plane. This results in an error of $1 - \cos \pi/6$ between the real curvilinear abscissa of the artery and the apparent one. The error in the wavelength measurement, and therefore in the phase velocity, is therefore 13%.

According to the new model of propagation derived from the Euler Bernoulli beam theory (21), the Young modulus E states as Eq. **4**, with v_f the flexural wave phase velocity, f the frequency, h the thickness of the artery, r its mean radius.

$$E = \frac{\rho v_f^4}{4\pi^2 f^2 hr}. \quad [4]$$

The main source of error comes from the distance estimate, contained in the phase velocity error. This induces an error of 50% on the Young modulus. We then estimate an error of 10% on the thickness due to the variation in the population. We also estimate an error of 20% on the radius due to local variation along the artery of interest. The error on the frequency is considered negligible compared with the other sources of error. The overall error on Young's modulus is estimated at 80%.

Data, Materials, and Software Availability. All study data are included in the article and/or supporting information. Previously published data were used for this work (29, 30).

ACKNOWLEDGMENTS. We would like to thank Tom Aubier for his helpful assistance with image processing tools, and Robin Genoud for his advice on angiographic techniques. This work was funded in part with financial support from Instituts Thématiques Multiorganismes Cancer of Aviesan within the framework of the 2021–2030 Cancer Control Strategy, on funds administered by French National Institute of Health and Medical Research. This work was also funded by l'Agence Nationale de la Recherche, Project ANR-24-CE19-4425.

1. T. Krouskop *et al*., A pulsed doppler ultrasonic system for making noninvasive measurements of the mechanical properties of soft tissue. *J. Rehabil. Res. Dev.* **24**, 1–8 (1987).
2. R. Muthupillai *et al*., Magnetic resonance elastography by direct visualization of propagating acoustic strain waves. *Science* **269**, 1854–1857 (1995).
3. A. Zorgani *et al*., Brain palpation from physiological vibrations using MRI. *Proc. Natl. Acad. Sci. U.S.A.* **112**, 12917–12921 (2015).
4. B. F. Kennedy, P. Wijesinghe, D. D. Sampson, The emergence of optical elastography in biomedicine. *Nat. Photonics* **11**, 215–221 (2017).
5. C. Zemzemi, J. Aichele, S. Catheline, Multiple sources array controls shear-wave field in soft tissue using time reversal. *Phys. Med. Biol.* **63**, 18NT02 (2018).
6. P. Hai, J. Yao, G. Li, C. Li, L. V. Wang, Photoacoustic elastography. *Opt. Lett.* **41**, 725–728 (2016).
7. P. Grasland-Mongrain *et al*., Ultrafast imaging of cell elasticity with optical microelastography. *Proc. Natl. Acad. Sci. U.S.A.* **115**, 861–866 (2018).
8. M. K. Badawy *et al*., Feasibility of using ultra-low pulse rate fluoroscopy during routine diagnostic coronary angiography. *J. Med. Radiat. Sci.* **65**, 252–258 (2018).
9. T. J. Hamilton *et al*., X-ray elastography: Modification of X-ray phase contrast images using ultrasonic radiation pressure. *J. Appl. Phys.* **105**, 102001 (2009).
10. J. G. Kim, S. E. Park, S. Y. Lee, X-ray strain tensor imaging: FEM simulation and experiments with a micro-CT. *J. X-Ray Sci. Technol.* **22**, 63–75 (2014).
11. C. Sutphin *et al*., Elastographic tomosynthesis from X-ray strain imaging of breast cancer. *IEEE J. Transl. Eng. Health Med.* **7**, 1–12 (2019).
12. C. Kamezawa *et al*., Dynamic X-ray elastography using a pulsed photocathode source. *Sci. Rep.* **11**, 24128 (2021).
13. K. S. Cheng, C. R. Baker, G. Hamilton, A. P. G. Hoeks, A. M. Seifalian, Arterial elastic properties and cardiovascular risk/event. *J. Vasc. Endovasc. Surg.* **24**, 383–397 (2002).
14. S. Laurent *et al*., Aortic stiffness is an independent predictor of all-cause and cardiovascular mortality in hypertensive patients. *Hypertension* **37**, 1236–1241 (2001).
15. G. Laloy-Borgna, L. Puyo, H. Nishino, M. Atlan, S. Catheline, Observation of natural flexural pulse waves in retinal and carotid arteries for wall elasticity estimation. *Sci. Adv.* **9**, eadf1783 (2023).
16. T. Young, I., The Croonian Lecture. On the functions of the heart and arteries. *Philos. Trans. R. Soc. Lond.* **99**, 1–31 (1809).
17. A. Milan *et al*., Current assessment of pulse wave velocity: Comprehensive review of validation studies. *J. Hypertens.* **37**, 1547–1557 (2019).
18. J. Luo, R. X. Li, E. E. Konofagou, Pulse wave imaging of the human carotid artery: An in vivo feasibility study. *IEEE Trans. Ultrason. Ferroelectr. Freq. Control* **59**, 174–181 (2012).
19. A. A. Isebree Moens, *Die Pulscurve* (E.J. Brill, Leiden, The Netherlands, 1878).
20. D. J. Korteweg, Ueber die fortpflanzungsgeschwindigkeit des schalles in elastischen röhren. *Ann. Phys. Chem.* **241**, 525–542 (1878).
21. S. Gregoire, G. Laloy-Borgna, J. Aichele, F. Lemoult, S. Catheline, Flexural pulse wave velocity in blood vessels. *J. Acoust. Soc. Am.* **155**, 2948–2958 (2024).
22. C. Collet *et al*., State of the art: Coronary angiography. *EuroIntervention* **13**, 634–643 (2017).
23. B. D. Lucas, T. Kanade, "An iterative image registration technique with an application to stereo vision" in *IJCAI'81: 7th International Joint Conference on Artificial intelligence* (1981), vol. 2, pp. 674–679.
24. N. M. Shapiro, M. Campillo, L. Stehly, M. H. Ritzwoller, High-resolution surface-wave tomography from ambient seismic noise. *Science* **307**, 1615–1618 (2005).
25. T. L. Duvall Jr, S. Jeffferies, J. Harvey, M. Pomerantz, Time-distance helioseismology. *Nature* **362**, 430–432 (1993).
26. F. Zvietcovich, P. Pongchalee, P. Meemon, J. P. Rolland, K. J. Parker, Reverberant 3D optical coherence elastography maps the elasticity of individual corneal layers. *Nat. Commun.* **10**, 4895 (2019).
27. R. Snieder, A. Grêt, H. Douma, J. Scales, Coda wave interferometry for estimating nonlinear behavior in seismic velocity. *Science* **295**, 2253–2255 (2002).
28. K. Wapenaar, D. Draganov, R. Snieder, X. Campman, A. Verdel, Tutorial on seismic interferometry: Part 1–Basic principles and applications. *Geophysics* **75**, 75A195–75A209 (2010).
29. R. Volleberg, S. van den Oord, R. J. Van Geuns, Hangover after side branch stenting: The discomfort comes afterwards. *Interventional Cardiol.: Rev., Res., Resour.* **17**, e08 (2022).
30. D. E. Drachman, D. M. Dudzinski, M.P. Moy, C. Fernandez-del Castillo, J. H. Chen, Case 27-2017. *N. Engl. J. Med.* **377**, 874–882 (2017), 10.1056/NEJMcpc1706111.
31. H. Kanai, Propagation of spontaneously actuated pulsive vibration in human heart wall and in vivo viscoelasticity estimation. *IEEE Trans. Ultrason. Ferroelectr. Freq. Control* **52**, 1931–1942 (2005).
32. M. Couade *et al*., In vivo quantitative mapping of myocardial stiffening and transmural anisotropy during the cardiac cycle. *IEEE Trans. Med. Imaging* **30**, 295–305 (2011).
33. B. Alan, S. Alan, Evaluation of carotid artery stiffness in patients with coronary artery disease using acoustic radiation force impulse elastography. *Vascular* **31**, 564–572 (2023).
34. G. L. Burke *et al*., Arterial wall thickness is associated with prevalent cardiovascular disease in middle-aged adults: The atherosclerosis risk in communities (ARIC) study. *Stroke* **26**, 386–391 (1995).
35. M. H. Kural *et al*., Planar biaxial characterization of diseased human coronary and carotid arteries for computational modeling. *J. Biomech.* **45**, 790–798 (2012).
36. A. Karimi, M. Navidbakhsh, A. Shojaei, S. Faghihi, Measurement of the uniaxial mechanical properties of healthy and atherosclerotic human coronary arteries. *Mater. Sci. Eng., C* **33**, 2550–2554 (2013).
37. X. Guo *et al*., Quantify patient-specific coronary material property and its impact on stress/strain calculations using in vivo IVUS data and 3D FSI models: A pilot study. *Biomech. Model. Mechanobiol.* **16**, 333–344 (2017).
38. Y. H. Wang *et al*., Reference values of the carotid elastic modulus using shear wave elastography and arterial stiffness change in coronary slow flow. *Eur. J. Radiol.* **157**, 110582 (2022).
39. S. Tu *et al*., In vivo assessment of optimal viewing angles from X-ray coronary angiography. *EuroIntervention* **7**, 112–120 (2011).

40. J. S. Chae, A. F. Brisken, G. Maurer, R. J. Siegel, Geometric accuracy of intravascular ultrasound imaging. *J. Am. Soc. Echocardiogr.* **5**, 577–587 (1992).
41. L. M. Zir, S. W. Miller, R. E. Dinsmore, J. P. Gilbert, J. W. Harthorne, Interobserver variability in coronary angiography. *Circulation* **53**, 627–632 (1976).
42. J. E. Galbraith, M. L. Murphy, N. de Soyza, Coronary angiogram interpretation: Interobserver variability. *JAMA* **240**, 2053–2056 (1978).
43. S. Çimen, A. Gooya, M. Grass, A. F. Frangi, Reconstruction of coronary arteries from X-ray angiography: A review. *Med. Image Anal.* **32**, 46–68 (2016).
44. K. R. Hoffmann, A. Wahle, C. Pellot-Barakat, J. Sklansky, M. Sonka, Biplane X-ray angiograms, intravascular ultrasound, and 3D visualization of coronary vessels. *Int. J. Cardiac Imaging* **15**, 495–512 (1999).
45. D. Jia, X. Zhuang, Learning-based algorithms for vessel tracking: A review. *Comput. Med. Imaging Graph.* **89**, 101840 (2021).
46. A. Scoccia *et al*., Angiography-based fractional flow reserve: State of the art. *Curr. Cardiol. Rep.* **24**, 667–678 (2022).
47. M. Többs *et al*., Comparison of fractional flow reserve based on computational fluid dynamics modeling using coronary angiographic vessel morphology versus invasively measured fractional flow reserve. *Am. J. Cardiol.* **117**, 29–35 (2016).
48. S. Catheline *et al*., Tomography from diffuse waves: Passive shear wave imaging using low frame rate scanners. *Appl. Phys. Lett.* **103**, 014101 (2013).
49. E. Larose *et al*., Correlation of random wavefields: An interdisciplinary review. *Geophysics* **71**, SI11-SI21 (2006).
50. L. Sandrin *et al*., Transient elastography: A new noninvasive method for assessment of hepatic fibrosis. *Ultrasound Med. Biol.* **29**, 1705–1713 (2003).
51. M. M. Kern, L. Gustafson, R. Kapur, S. Wasek, Angiographic projections made simple: An easy guide to understanding oblique views. *Cath Lab Digest* **19**, 8 (2011).